

PHOTONICS Research

Fully integrated and broadband Si-rich silicon nitride wavelength converter based on Bragg scattering intermodal four-wave mixing

VALERIO VITALI,^{1,2,*} THALÍA DOMÍNGUEZ BUCIO,¹ HAO LIU,¹ JOSÉ MANUEL LUQUE GONZÁLEZ,³ FRANCISCO JURADO-ROMERO,³ ALEJANDRO ORTEGA-MOÑUX,³ GLENN CHURCHILL,¹ JAMES C. GATES,¹ JAMES HILLIER,^{4,5} NIKOLAOS KALFAGIANNIS,^{4,6} DANIELE MELATI,⁷ JENS H. SCHMID,⁸ ILARIA CRISTIANI,² PAVEL CHEBEN,⁸ J. GONZALO WANGÜEMERT-PÉREZ,³ ÍÑIGO MOLINA-FERNÁNDEZ,³ FREDERIC GARDES,¹ COSIMO LACAVA,² AND PERIKLIS PETROPOULOS¹

¹Optoelectronics Research Centre, University of Southampton, Southampton, SO17 1BJ, UK

²Electrical, Computer and Biomedical Engineering Department, University of Pavia, Pavia, 27100, Italy

³Telecommunication Research Institute (TELMA), Universidad de Málaga, CEI Andalucía TECH, E.T.S.I. Telecomunicación, 29010 Málaga, Spain

⁴School of Science and Technology, Nottingham Trent University, Nottingham, NG11 8NS, UK

⁵Department of Electrical Engineering, Eindhoven University of Technology, Eindhoven, 5600 MB, The Netherlands

⁶Department of Materials Science and Engineering, University of Ioannina, Ioannina 45110, Greece

⁷Centre de Nanosciences et de Nanotechnologies, Université Paris-Saclay, CNRS, 91120 Palaiseau, France

⁸Advanced Electronics and Photonics Research Center, National Research Council Canada, 1200 Montreal Road, Ottawa,

Ontario K1A 0R6, Canada

*Corresponding author: valerio.vitali@unipv.it

Received 22 September 2023; revised 12 November 2023; accepted 13 November 2023; posted 21 November 2023 (Doc. ID 506691); published 0 MONTH 0000

Intermodal four-wave mixing (FWM) processes have recently attracted significant interest for all-optical signal processing applications thanks to the possibility to control the propagation properties of waves exciting distinct spatial modes of the same waveguide. This allows, in principle, to place signals in different spectral regions and satisfy the phase matching condition over considerably larger bandwidths compared to intramodal processes. However, the demonstrations reported so far have shown a limited bandwidth and suffered from the lack of on-chip components designed for broadband manipulation of different modes. We demonstrate here a silicon-rich silicon nitride wavelength converter based on Bragg scattering intermodal FWM, which integrates mode conversion, multiplexing and de-multiplexing functionalities on-chip. The system enables wavelength conversion between pump waves and a signal located in different telecommunication bands (separated by 60 nm) with a 3 dB bandwidth exceeding 70 nm, which represents, to our knowledge, the widest bandwidth ever achieved in an intermodal FWM-based system. © 2023 Chinese Laser Press

<https://doi.org/10.1364/PR.506691>

32 1. INTRODUCTION

33 Present optical transmission systems need to cope with an ever-
34 growing demand for bandwidth to transmit the continuously
35 growing amount of data generated across the world. A para-
36 digm shift in optical networks and photonic devices will be re-
37 quired to tackle this challenge and increase the efficiency of the
38 current wavelength division multiplexing (WDM)-based opti-
39 cal communication systems [1]. While techniques based on
40 space division multiplexing hold significant promise [2–4], a
41 complementary attractive route to increasing the capacity of
42 optical networks comes from the observation that current sys-
43 tems make use of only a small portion of the wide low-loss
44 bandwidth of silica optical fibers. In this regard, configurations

45 that exploit optical wavelength bands outside the conventional
46 C-band spectrum (1530–1565 nm) are currently being investi-
47 gated [5,6]. One particularly attractive option is represented
48 by the use of the adjacent L- (1565–1625 nm) and U-bands
49 (1625–1675 nm). Similar to the C-band, in these new systems,
50 the ability to generate, convert and manipulate optical signals is
51 highly desirable. Third-order-nonlinearity-based optical devices
52 could be used to generate and convert wavelength components
53 through well-studied parametric optical processes such as those
54 based on four-wave mixing (FWM) [7]. Various demonstra-
55 tions have already been reported for the realization of wave-
56 length converters and synthesizers capable of operating over
57 a broad wavelength range, mainly based on the use of integrated

waveguides [8–10]. In general, most of these demonstrations have exploited nonlinear processes based on intramodal FWM, i.e., where all the waves propagate in the same optical spatial mode. More recently, integrated systems based on intermodal FWM (IM-FWM) processes, i.e., where the involved waves propagate in different spatial modes of the same waveguide, have been studied, and have shown considerable potential to respond to the requirements of next-generation communication systems. Indeed, the introduction of additional modes in nonlinear waveguides offers an extra degree of freedom in dispersion engineering to fulfil the required phase matching condition thanks to the possibility of tuning the characteristics of distinct spatial modes over the wavelengths of interest. This allows in principle for broadband operation in multiple spectral bands of the electromagnetic spectrum, even located hundreds of nanometers away from the pump source(s) [11,12]. Several demonstrations of IM-based applications have already been shown, such as supercontinuum generation [13–15], comb generation [16,17], signal processing based on stimulated IM Brillouin scattering [18,19], wavelength conversion [12,20–24] and the realization of photon pair sources for quantum applications [25–27]. Most of these demonstrations made use of either degenerate or non-degenerate parametric amplification, where the idler generation is accompanied by the amplification of vacuum fluctuations, which inherently adds excess noise to the process [28,29]. However, in both the classical and quantum regimes, minimum excess noise is desirable since additional noise can result in higher bit-error rates in classical telecommunication systems and poor fidelity of translated quantum states in quantum systems [30,31]. An alternative non-degenerate FWM process, termed Bragg scattering (BS) FWM, does not amplify vacuum fluctuations and, therefore, can in principle convert photons from the signal to the idler frequency without excess noise [30,32]. Some promising wavelength converters implementing a BS-IM-FWM configuration have already been reported in the C- and L-bands using integrated waveguides [20,21]. These first demonstrations showed the potential of the BS-IM-FWM process; however, their experimental implementations were complex and suffered from the lack of integrated components for manipulating the spatial shapes of the involved optical modes on-chip, eventually adding further losses to the whole system. As a consequence, this limited the conversion efficiency of the proposed devices, even when relatively high pump power levels were employed, and, ultimately, the achievable bandwidth due to the use of bulky off-chip components to manipulate the involved optical modes.

In this paper, we present the design and experimental characterization of a fully integrated and broadband wavelength converter based on the use of the BS-IM-FWM process implemented on a silicon-rich silicon nitride (Si-rich SiN) platform. The system integrates the whole set of functionalities required to perform frequency conversion on-chip in the IM regime, starting from three seeding waves (two pumps and one signal), which are coupled from an array of lensed single-mode optical fibers. This eliminates the requirement for external and bulky mode conversion, multiplexing and demultiplexing elements, significantly reduces the insertion losses of the whole system and eliminates the need of filtering out the optical pumps at

the device output. The proposed device is capable of generating idler wavelengths covering the range of 1600–1678 nm starting from a seeding signal at 1600 nm, with an experimentally measured 3 dB bandwidth greater than 70 nm, by utilizing optical pumps located in the wavelength range of 1540–1616 nm. To the best of the authors' knowledge, this represents the widest bandwidth ever achieved in a multimode FWM-based device.

2. BRAGG SCATTERING INTERMODAL FWM SCHEME

A general illustration of the BS-FWM process is shown in Fig. 1(a). As can be seen, BS-FWM enables the generation of blue and red shifted copies ($I_{BS,b}$ and $I_{BS,r}$ idlers, respectively) of the seeding signal (S) through a scattering process induced by an intensity grating caused by the interference between the two pumps (P_1 and P_2). The values of the idler frequencies are determined by the energy conservation law, i.e., they appear at $\omega_S \pm \Delta\omega$, where ω_S stands for the signal frequency and $\Delta\omega$ is the frequency difference between the two pumps. As in any FWM-based process, efficient conversion is ensured only when the interacting waves satisfy the phase matching condition. This can generally be achieved only for one idler at a time, and, in most cases, the other non-phase-matched idler

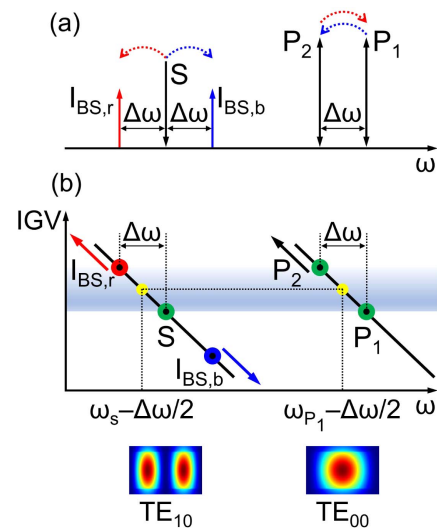


Fig. 1. (a) Dual-pump BS FWM working principle. When two pumps (P_1 and P_2) and a seeding signal (S) are input into a third-order nonlinear waveguide, BS FWM can occur under the assumption that the phase matching condition is fulfilled. In this scenario, photons are scattered from the signal S to two idlers ($I_{BS,b}$ and $I_{BS,r}$), with a simultaneous energy exchange between the two pumps. The solid arrows indicate the loss (down) and gain (up) of the photon energy, while the dashed arrows indicate the direction of the energy exchange for the $I_{BS,r}$ (red) and $I_{BS,b}$ (blue) cases. (b) Graphical illustration of the phase matching mechanism for the BS-IM-FWM scheme. If P_1 and P_2 are placed in the TE_{00} mode and the signal and idlers in the TE_{10} mode of a multimode waveguide, the phase matching condition can be satisfied and retained if it is possible to draw a horizontal line that crosses the IGV curves of the two considered modes at the average frequencies (yellow dots in the figure) of the two pumps and of the signal and one idler (either $I_{BS,b}$ or $I_{BS,r}$).

represents an unwanted by-product of the nonlinear process. In the case of single-mode waveguides, phase matching is commonly accomplished by carefully designing the waveguide geometry to engineer the group velocity dispersion [33]. Specifically, in order to achieve efficient BS FWM, the waveguide needs to exhibit zero dispersion at the half-distance between the average frequency of the signal–idler pair and that of the pair of pumps [30,34]. However, in the IM regime, the phase matching condition gives rise to different requirements. An illustrative schematic of the operating principle to satisfy the phase matching condition in the BS-IM-FWM configuration is illustrated in Fig. 1(b) [20,35,36], which shows the inverse group velocity (IGV) curves of two distinct spatial modes supported in a multimode waveguide as a function of the angular frequency ω . The inverse group velocity is defined as $IGV = v_g^{-1} = n_g/c$, where v_g is the group velocity, n_g is the group index and c is the speed of light in vacuum.

In our simulations and experiments, P_1 and P_2 were placed into the fundamental TE-polarized waveguide mode (TE_{00}), while the signal S and the generated idlers $I_{BS,b}$ and $I_{BS,r}$ were in the first-order TE-polarized horizontal mode (TE_{10}). Considering the $I_{BS,r}$ idler, phase matching is ensured when the following equation is fulfilled [20]:

$$-\beta^0(\omega_{P1}) + \beta^1(\omega_S) + \beta^0(\omega_{P2}) - \beta^1(\omega_{BS,r}) = 0, \quad (1)$$

where $\beta^0(\omega)$ and $\beta^1(\omega)$ are the propagation constants of the TE_{00} and TE_{10} modes at the angular frequency ω , respectively, and ω_{P1} , ω_{P2} , ω_S and $\omega_{BS,r}$ stand for the angular frequencies of pump 1, pump 2, signal and red shifted BS idler, respectively. Equation (1) can be rewritten as

$$\beta^0(\omega_{P1}) - \beta^0(\omega_{P1} - \Delta\omega) = \beta^1(\omega_S) - \beta^1(\omega_S - \Delta\omega). \quad (2)$$

Under the assumption of a small frequency detuning ($\Delta\omega \approx 0$), Eq. (2) shows that phase matching is satisfied when the derivative function of the propagation constant in one mode (β^0), which is its IGV, evaluated at the P_1 frequency ω_{P1} , is equal to the derivative function of the propagation constant in the other mode (β^1), calculated at the signal frequency ω_S . Therefore, any possible frequency combinations to achieve phase matching across the two modes (or various modes, in case higher-order modes are also considered) can be found by the crossing of any horizontal line drawn on the IGV curves of Fig. 1(b). For a greater $\Delta\omega$ detuning, if P_2 is tuned towards shorter frequencies, $\omega_{BS,r}$ moves in the same direction, and it is still possible to draw an upshifted horizontal line crossing the two IGV curves at the new average frequencies ($\omega_{P1} - \Delta\omega/2$ and $\omega_S - \Delta\omega/2$), provided that each IGV curve is a frequency-shifted replica of the other. Conversely, the $I_{BS,b}$ idler component, even though it satisfies the energy conservation principle as $I_{BS,r}$, is shown to not satisfy the phase matching condition in the reported example because it is only possible to draw an oblique line to cross the two IGV points at the new average frequencies. As the P_2 detuning to lower frequencies increases, $I_{BS,b}$ moves further away from phase matching. It should be noted that if the P_1 frequency is tuned to higher ω values, the opposite scenario holds true: a broadband operation can be achieved for $I_{BS,b}$, whereas $I_{BS,r}$ quickly moves away from phase matching as $\Delta\omega$ increases. The presented phase matching mechanism can be exploited to efficiently

suppress one idler component to achieve a unidirectional FWM process, as already demonstrated in [20]. Interestingly, this scheme can be applied to any pair of supported waveguide modes. When a higher-order mode is considered, the frequency separation between the pumps and the signal–idlers can be further increased. Therefore, provided that the IGV curves of the considered modes meet the criteria described above, the phase matching condition can still be satisfied even for extremely large pump-to-signal frequency detuning values. The described properties of the BS-IM-FWM differ significantly from the ones of the single-mode case and pose less stringent requirements on the engineering of the dispersion and dispersion slope profiles of the waveguide, thus providing more flexibility on the design of wavelength converters, especially when a large wavelength detuning is desirable.

3. NONLINEAR MULTIMODE WAVEGUIDE DESIGN

The nonlinear multimode waveguide was designed for our in-house Si-rich SiN platform, consisting of a Si-rich SiN strip waveguide surrounded by a silicon dioxide (SiO_2) cladding. This material platform allows excellent dispersion engineering control and precise tuning of the propagation characteristics of the supported modes by varying the waveguide geometry and the refractive index of the core material itself, which can be controlled by changing the Si-rich SiN deposition conditions [37]. In addition, the material can be engineered to show a high Kerr coefficient with no two-photon absorption (TPA)-related losses in the telecommunication bands [38]. Figure 2 shows the cross-section of the designed waveguide (6.1 μm width \times 310 nm height) and the simulated group index n_g curves as a function of wavelength λ for the first two considered modes (TE_{00} and TE_{10}). The refractive index of the Si-rich SiN core material (Si_xN_y) was set equal to 2.41 at 1550 nm by adjusting the silicon content within the silicon nitride host matrix in the deposition process [37]. The waveguide cross-section was engineered to achieve the phase matching condition between the TE_{00} and TE_{10} modes at wavelengths $\lambda_{TE00} = 1540$ nm and $\lambda_{TE10} = 1600$ nm, respectively. In our experiments, the two

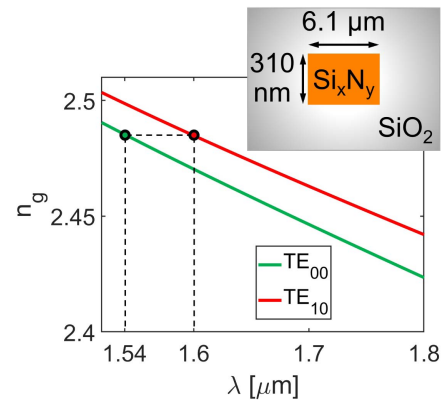


Fig. 2. Numerically simulated group index n_g for the first two horizontal modes TE_{00} and TE_{10} as a function of wavelength λ and sketch of the cross-section of the Si-rich SiN multimode waveguide employed in this work (note that dimensions are not to scale).

194
195
196
197
198
199
200
201
202
203
204
205
206
207
208
209
210
211
212
213
214
215
216
217
218
219
220
221
222
223
224
225
226
227
228
229
230
231
F2:1
F2:2
F2:3
F2:4

232 pumps P_1 and P_2 were placed in the TE_{00} mode, while the
 233 signal S and the generated idlers were in the TE_{10} mode. As
 234 can be seen from Fig. 2, the nonlinear multimode waveguide
 235 was designed so that the two n_g curves, which are proportional
 236 to the IGV curves, are a frequency-shifted replica of each other
 237 to ensure a wide conversion bandwidth.

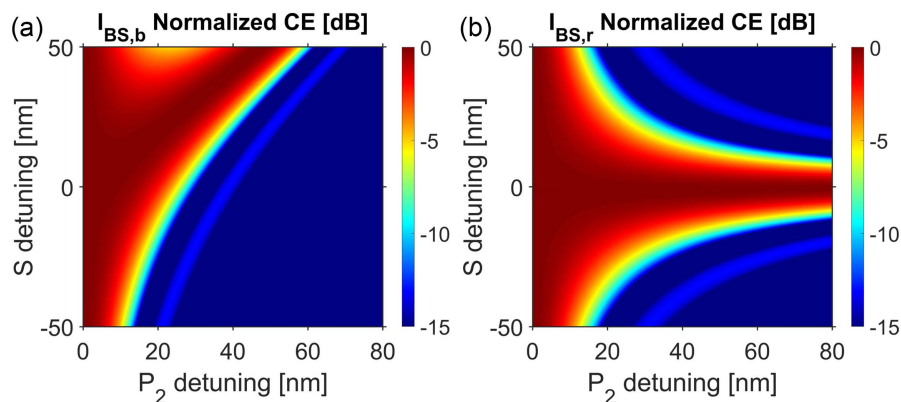
238 By considering this specific mode and wavelength configura-
 239 tion, the bandwidth of the BS-IM-FWM process in terms of
 240 conversion efficiency (CE) for both $I_{BS,b}$ and $I_{BS,r}$ was numeri-
 241 cally calculated as a function of the pump and signal wavelength
 242 detuning. The CE was defined as $CE = P_I(L_{MM})/P_S(L_{MM})$,
 243 where $P_I(L_{MM})$ is the optical power of the $I_{BS,b}$ or $I_{BS,r}$ idlers
 244 and $P_S(L_{MM})$ is the signal S power evaluated at the output
 245 of the nonlinear multimode waveguide (with length L_{MM}),
 246 respectively. The two waveguide modes and their dispersion
 247 profiles were numerically calculated using a Finite Difference
 248 Eigenmode (FDE) solver from MODE Solutions (Ansys
 249 Inc.). For the Si-rich SiN core, the refractive index profile
 250 was experimentally acquired via infrared (IR) spectroscopic el-
 251 lipsometry measurements performed on the bulk material em-
 252 ployed in this work, while the data reported by Palik were used
 253 for the SiO_2 cladding [39]. The numerically simulated modal
 254 effective index profiles and mode overlap factors were used for
 255 nonlinear wave propagation simulations based on the fourth-
 256 order Runge–Kutta method [40]. Further details about the
 257 coupled equations used to model the BS-IM-FWM process
 258 can be found in [21]. The nonlinear Kerr coefficient was set
 259 to $n_2 = 1.56 \cdot 10^{-18} \text{ m}^2/\text{W}$, which was experimentally mea-
 260 sured as described in [37], while the nonlinear waveguide
 261 length was set equal to $L_{MM} = 1 \text{ cm}$. A propagation loss co-
 262 efficient $\alpha = 2.3 \text{ dB/cm}$ was considered. In these simulations,
 263 the wavelength of P_1 was kept fixed at 1540 nm, while the
 264 wavelengths of P_2 and signal S were varied. In all cases, the
 265 total pump power level was kept at 27.6 dBm (24.6 dBm
 266 per pump), while the signal power was set at 8 dBm, as in
 267 the nonlinear experiments. Figure 3 reports the normalized
 268 CE results from the numerical simulations for the $I_{BS,b}$ and
 269 $I_{BS,r}$ in Figs. 3(a) and 3(b), respectively. By considering a
 270 signal-detuning close to zero (corresponding to the signal set
 271 close to the nominal designed wavelength $\lambda_S = 1600 \text{ nm}$), an
 272 (almost) constant CE level can be obtained for $I_{BS,r}$ even for

273 extremely large P_2 detuning values ($>80 \text{ nm}$). On the other
 274 hand, $I_{BS,b}$ is hindered in this scenario, and phase matching
 275 is only achieved over a significantly narrower P_2 detuning range
 276 compared to the $I_{BS,r}$ case. In addition, Fig. 3(b) also shows
 277 that even for P_2 detuning values as large as 30 nm, the
 278 conversion process to $I_{BS,r}$ is (almost) insensitive to the signal
 279 wavelength for a signal-detuning bandwidth of $\approx 18 \text{ nm}$
 280 around $\lambda_S = 1600 \text{ nm}$, with no significant degradation in
 281 CE ($<1 \text{ dB}$ variation).

282 The fabrication tolerance of the nonlinear multimode wave-
 283 guide was then evaluated to estimate the impact of dimension
 284 variations on the position of the phase-matched signal wave-
 285 length relative to the nominal design value of 1600 nm. By
 286 considering a $\pm 30 \text{ nm}$ variation of the waveguide width and
 287 thickness, shifts of approximately $\mp 1 \text{ nm}$ and $\pm 9 \text{ nm}$ in
 288 the position of the phase-matched signal wavelength were
 289 found, respectively, showing good fabrication tolerance. As dis-
 290 cussed in the previous section, the use of higher-order modes
 291 would allow, in principle, to achieve an even larger separation
 292 between the pumps and signal–idler pairs. For example, con-
 293 sidering the multimode waveguide cross-section used in this
 294 work ($6.1 \mu\text{m}$ width \times 310 nm height), by setting the two
 295 pumps in the TE_{00} mode with P_1 fixed at 1540 nm, the
 296 phase-matched signal wavelengths would move to $\approx 1730 \text{ nm}$
 297 and $\approx 2110 \text{ nm}$ when the TE_{20} and TE_{30} modes are employed
 298 for the signal–idler pairs, respectively. The use of higher-order
 299 modes would require a modification of the design of the differ-
 300 ent components for mode conversion and manipulation at
 301 longer wavelengths, which may be of interest for future studies
 302 targeting mid-infrared (MIR) frequency generation.

4. DEVICE LAYOUT AND WORKING PRINCIPLE 303

304 A schematic layout of the full device and its working principle is
 305 shown in Fig. 4. The system consists of five different blocks:
 306 input section, mode converter and multiplexer (mode-MUX),
 307 nonlinear multimode waveguide, mode converter and demul-
 308 tiplexer (mode-DEMUX) and output section. In the input sec-
 309 tion, inverted-taper-based edge couplers (ECs) were designed to
 310 efficiently couple signals incoming from lensed single-mode
 311 polarization-maintaining (PM) optical fibers. A two-fiber array



F3:1 **Fig. 3.** Simulated BS-IM-FWM normalized CE for different P_2 and S detuning values for (a) $I_{BS,b}$ and (b) $I_{BS,r}$. The P_1 wavelength was set
 F3:2 equal to $\lambda_{P1} = 1540 \text{ nm}$ for all the considered cases. The phase matching wavelength for the signal S is $\lambda_S = 1600 \text{ nm}$ (which corresponds to a
 F3:3 signal-detuning equal to zero).

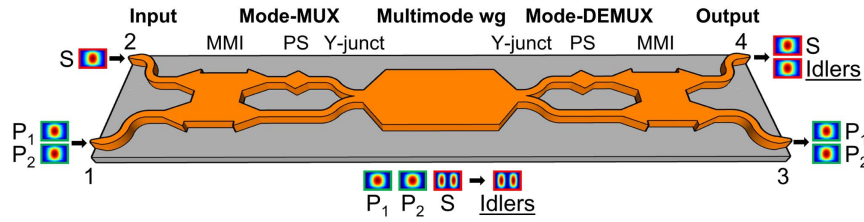


Fig. 4. Schematic layout and working principle of the fully integrated intermodal FWM-based wavelength converter. P_1 , pump 1; P_2 , pump 2; S , signal; MMI, multimode interference coupler; PS, phase shifter; Y-junct, Y-junction; mode-MUX, mode converter and multiplexer; wg, waveguide; mode-DEMUX, mode converter and demultiplexer.

(FA) was used to simultaneously couple the two pumps (P_1 and P_2) into port 1 of the device and the signal (S) into port 2. The ECs were connected to the mode-MUX through bent single-mode waveguides. The mode-MUX comprised a multimode interference (MMI) coupler, a 90° phase shifter (PS) and a sinusoidal-profile symmetric Y-junction (overall footprint of the mode-MUX: $4 \mu\text{m} \times 121 \mu\text{m}$). The mode-MUX was designed according to the following working principle [41,42]: a TE_{00} mode input from port 1 was equally split by the MMI and a $+90^\circ$ phase shift was induced between the modes propagating through the MMI upper and lower output arms. Afterwards, the PS introduced a -90° phase shift between the mode propagating through the upper arm relative to the mode propagating through the lower arm, eliminating the phase difference between the two optical modes. Hence, two in-phase TE_{00} modes reached the symmetric Y-junction and underwent conversion into the fundamental TE_{00} mode of the multimode waveguide. Conversely, a TE_{00} mode coupled into port 2 was also equally split by the MMI, but, in this case, a -90° phase shift was induced between the modes propagating through the MMI upper and lower output arms. Therefore, after propagating through the PS section, two out-of-phase (180° overall phase shift) TE_{00} modes reached the symmetric Y-junction and underwent conversion to the TE_{10} mode of the multimode waveguide. In this manner, the two pumps coupled in from port 1 excited the TE_{00} mode of the multimode waveguide, while the signal coupled in from port 2 excited the TE_{10} mode. The BS-IM-FWM process then occurred in the multimode waveguide (length $L_{\text{MM}} = 1 \text{ cm}$, whole device length = 1.14 cm) with the generation of $I_{\text{BS},b}$ and $I_{\text{BS},r}$ idlers in the TE_{10} mode. Next, a mode-DEMUX and output section performed the reciprocal operation of the input section and mode-MUX. The two residual pump waves were maintained in the

TE_{00} mode and coupled out from port 3, while the signal and idler waves in the TE_{10} mode were converted to the TE_{00} mode by the mode-DEMUX and coupled out from port 4. As at the side of the input, a two-fiber array was used to simultaneously couple out all the waves from the two output ports. It is worth noticing that this configuration allowed separating the signal and idler waves from the two optical pumps, therefore eliminating by design the requirement to filter the high-power pumps out from the desired signals. The geometrical dimensions of the designed device are listed in Appendix A.

5. FABRICATION

The proposed device was fabricated on a 200 mm Si wafer with a $3 \mu\text{m}$ thermally grown oxide layer as a starting substrate. The 310 nm thick Si-rich SiN device layer, with a refractive index of 2.41 at 1550 nm , was deposited at a low processing temperature (350°C) using an NH_3 -free plasma enhanced chemical vapor deposition (PECVD) process, as detailed in [37,43]. Afterwards, the test structures were patterned with a 248 nm deep-UV (DUV) lithography tool using a 680 nm thick positive tone resist mask with a 60 nm thick bottom anti-reflection coating (BARC). The BARC layer was included to reduce the sidewall roughness generated by the back-reflected light during the lithography process, which can have a detrimental effect on the propagation losses of the fabricated devices. The pattern was then transferred onto the Si-rich SiN layer by means of an inductively coupled plasma (ICP) etching process using an $\text{SF}_6:\text{C}_4\text{F}_8$ chemistry with an etching depth of 310 nm . The resist mask was then removed using an O_2 plasma process and an RCA-1 cleaning step. Finally, a $2 \mu\text{m}$ thick PECVD SiO_2 layer was deposited as cladding. Figure 5 shows a schematic diagram of the device along with scanning electron microscope (SEM) images of the top-view of the MMI [Fig. 5(a)],

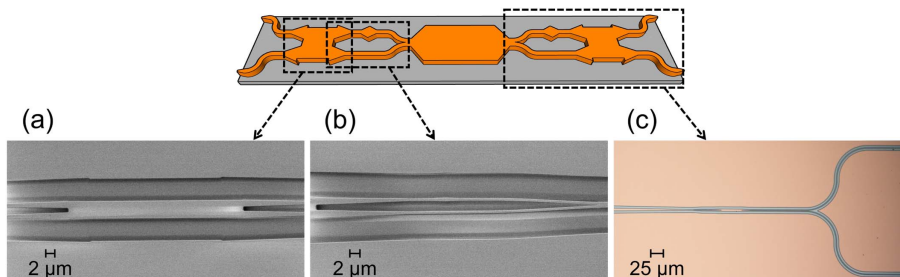


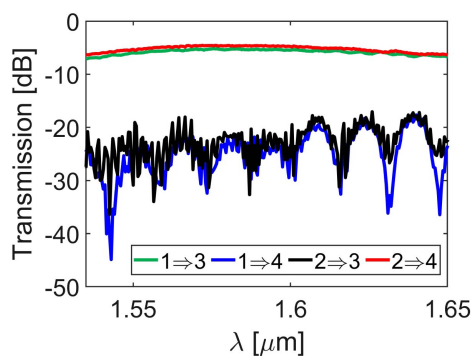
Fig. 5. Schematic layout of the fabricated device along with top-view SEM images of (a) MMI, (b) PS and Y-junction sections of the mode-MUX and (c) an optical microscope image of the full mode-DEMUX and output section.

377 PS and Y-junction [Fig. 5(b)] sections of the device and an optical
378 microscope image of the full mode-DEMUX and output
379 section [Fig. 5(c)].

380 The input and output facets were prepared by dicing, a type
381 of mechanical sawing that uses diamond grit-impregnated
382 blades, traditionally employed to separate individual dies from
383 a wafer. Through careful selection of blade composition and
384 cutting parameters, ductile removal of optical materials can
385 be achieved, resulting in sub-nanometer roughness [44].
386 High-quality facets with negligible chipping and delamination
387 of material layers were produced in a single step with no re-
388 quirement for time-consuming polishing [45]. The coupling
389 losses per facet between a lensed single-mode PM optical fiber
390 (spot diameter of 3.5 μm) and the inverted-taper-based EC
391 were assessed to be 1.4 dB, while the propagation losses of
392 the nonlinear multimode waveguide were measured to be equal
393 to 2.3 dB/cm at 1550 nm.

394 6. EXPERIMENTAL RESULTS

395 The linear performance of the full device was initially evaluated.
396 Figure 6 shows the measured fiber-to-fiber transmission curves
397 between the two input ports (1, 2) and output ports (3, 4).
398 Considering the transmission curves between ports 1 to 3 (in-
399 put: TE_{00} , multimode waveguide: TE_{00} , output: TE_{00}) and
400 ports 2 to 4 (input: TE_{00} , multimode waveguide: TE_{10} , output:
401 TE_{00}), a minimum fiber-to-fiber loss of ≈ 5 dB was measured
402 around 1580 nm, with a maximum variation lower than 2 dB
403 in the measured wavelength range 1535–1650 nm. The un-
404 wanted transmission between crossing input–output ports



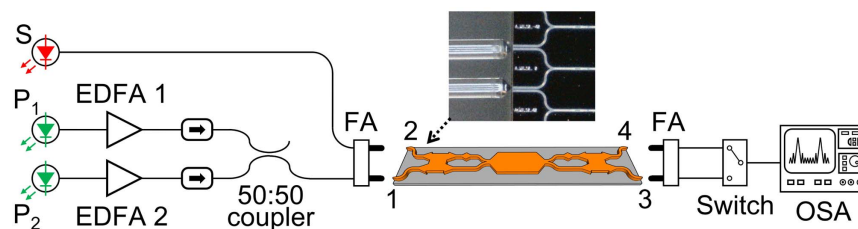
F6:1 **Fig. 6.** Linear characterization of the full device: measured transmis-
F6:2 sion curves as a function of wavelength for the different combinations
F6:3 of input–output ports.

(ports 1 to 4 and ports 2 to 3) was also measured, resulting
405 in a minimum loss value of 17 dB. Overall, the device shows
406 a crosstalk value lower than -10 dB between direct and crossing
407 port-to-port transmissions in the measured wavelength range.
408 Considering the individual components, the full device band-
409 width and crosstalk performance are ultimately limited by the
410 spectral response of the tapered 90° PS, which also represents
411 the most sensitive element to fabrication imperfections. In order
412 to reduce the device crosstalk and expand the operational
413 bandwidth, the use of subwavelength grating PSs could be con-
414 sidered. These structures have also shown greater robustness to
415 fabrication errors compared to conventional devices, as already
416 demonstrated in previous works [46,47].

417 Nonlinear measurements were then carried out using the
418 setup shown in Fig. 7. The continuous wave (CW) optical
419 pumps (P_1 and P_2) were generated using two PM tunable laser
420 sources (TLSs) followed by two PM erbium-doped fiber ampli-
421 fiers (EDFAs). The pumps, after passing through two optical
422 isolators, were coupled together with a 50:50 PM fiber coupler
423 and sent to port 1 of the integrated device. The signal (S) was
424 generated using a third PM TLS and directly sent to port 2 of
425 the integrated device. At the device output, the two residual
426 pumps on port 3 along with the signal and idlers on port 4
427 were collected and sent to an optical spectrum analyzer (OSA)
428 using an optical switch. One input and one output FA with two
429 lensed PM optical fibers each were used to couple the signals in
430 and out of the device.

431 Two different sets of nonlinear experiments were performed
432 using a total pump power of 27.6 dBm (24.6 dBm per pump)
433 and a signal power of 8 dBm coupled into the chip. In the first
434 set of measurements, the first pump P_1 was set at 1540 nm (as
435 in the numerical simulations), while the wavelength of the sec-
436 ond pump P_2 was scanned from 1542 to 1616 nm in order to
437 characterize the pump-to-pump detuning bandwidth of the
438 BS-IM-FWM process for both the $I_{\text{BS},b}$ and $I_{\text{BS},r}$ idlers.
439 According to the previously presented numerical simulations,
440 the signal S was placed at 1600 nm in order to ensure phase
441 matching with P_1 . Figure 8(a) reports the CE measured for the
442 $I_{\text{BS},b}$ (blue squares) and $I_{\text{BS},r}$ (red diamonds) idlers as a function
443 of the pump-to-pump detuning $\Delta\lambda_{\text{pp}}$.

444 A small CE decrease for increasing $\Delta\lambda_{\text{pp}}$ can be observed for
445 $I_{\text{BS},r}$, with a 3 dB pump-to-pump detuning bandwidth of
446 72 nm, corresponding to an idler generated in the range of
447 1602–1678 nm. Conversely, as expected, a much narrower
448 3 dB pump-to-pump detuning bandwidth of ≈ 20 nm was
449 measured for $I_{\text{BS},b}$. Numerical simulations were carried out
450



F7:1 **Fig. 7.** Sketch of the experimental setup used in the nonlinear experiments. P_1 , pump 1; P_2 , pump 2; S , signal; EDFA, erbium-doped fiber
F7:2 amplifier; FA, fiber array; OSA, optical spectrum analyzer. The inset shows a microscope image of the optical coupling between the input FA and the
F7:3 on-chip integrated device.

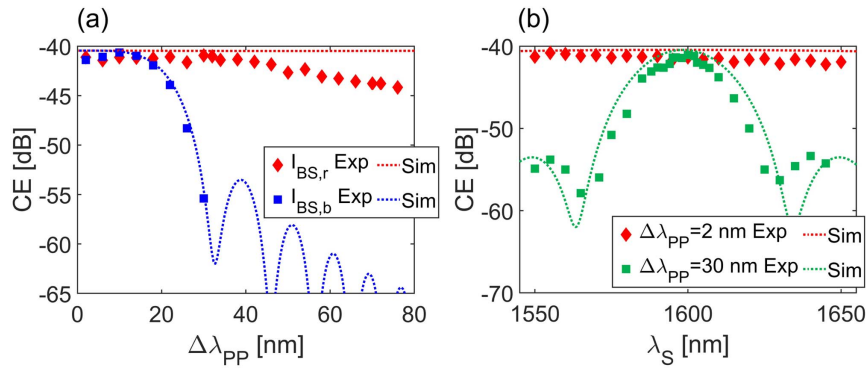


Fig. 8. (a) Experimentally measured CE for the $I_{BS,r}$ (red diamonds) and $I_{BS,b}$ (blue squares) idlers and corresponding numerically simulated CE (red and blue dashed lines, respectively) as a function of the P_2 detuning with P_1 and S wavelengths fixed at 1540 and 1600 nm, respectively. (b) Experimentally measured CE for the $I_{BS,r}$ idler as a function of the signal wavelength λ_S for a P_2 detuning of 2 nm (red diamonds, pump-to-pump detuning $\Delta\lambda_{pp} = 2$ nm) and 30 nm (green squares, $\Delta\lambda_{pp} = 30$ nm) and corresponding numerically simulated CE (red and green dashed lines, respectively), with P_1 wavelength fixed at 1540 nm.

by considering the pump power values used in the experiments and the measured propagation losses of the multimode waveguide, with the results reported in Fig. 8(a) (blue and red dashed lines for $I_{BS,b}$ and $I_{BS,r}$, respectively) showing a good agreement with the experimental results. The decrease in the experimentally measured $I_{BS,r}$ CE observed for the greater $\Delta\lambda_{pp}$ detuning values can be mainly attributed to the linear transfer function of the full device (see ports 2 to 4 curve in Fig. 6, which shows a decreasing transmission for longer wavelengths in the L- and U-bands). Three examples of optical spectra measured at port 4 are reported in Figs. 9(a)–9(c) for P_2

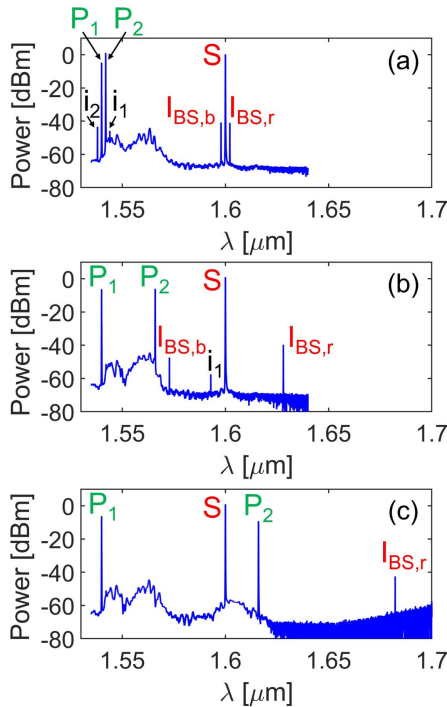


Fig. 9. Optical spectra measured at port 4 for P_2 detuning values $\Delta\lambda_{pp}$ of (a) 2 nm, (b) 26 nm and (c) 76 nm. The wavelengths of P_1 and S are set at 1540 and 1600 nm, respectively.

detuning values of 2, 26 and 76 nm, respectively. As can be seen, an almost constant power level for $I_{BS,r}$ was recorded for the three different P_2 detuning values. Despite the total pump power being significantly (≈ 20 dB) higher than the signal power at the chip input, the power level measured at port 4 for the two pumps, P_1 and P_2 , is comparable to that of the signal S , since most of the power of the two pumps is sent to port 3. It is also noteworthy that, for small P_2 detuning values [e.g. Figs. 9(a) and 9(b)], intra-modal FWM components are also generated (i_1 and i_2), which result from the degenerate FWM process between the two pumps (both of them placed in the TE_{00} mode).

In the second measurement campaign, the signal-detuning bandwidth was evaluated: P_1 and P_2 were initially placed at 1540 and 1542 nm ($\Delta\lambda_{pp} = 2$ nm), respectively, while the signal wavelength was varied between 1550 and 1650 nm. Using this wavelength setting, the CE values for the $I_{BS,r}$ idler were measured. The results are reported in Fig. 8(b) (red diamonds) and show no significant CE decrease, even for a large signal-detuning of ± 50 nm relative to the predicted central signal wavelength of 1600 nm. The experiments were then repeated placing P_1 and P_2 at 1540 and 1570 nm ($\Delta\lambda_{pp} = 30$ nm), respectively, and the resulting CE values for the $I_{BS,r}$ idler are reported in Fig. 8(b) (green squares). In this configuration, the phase matching was not retained across the entire range of scanned signal wavelengths, and a 3 dB signal-detuning bandwidth of ≈ 25 nm was measured, centered at around 1600 nm. Even in this case, the experimental results are in good agreement with numerical simulations [see Fig. 8(b), red and green dashed lines for pump-to-pump detuning values of 2 and 30 nm, respectively], confirming that the nonlinear multimode waveguide showed a low dispersion value. This enabled flexible positioning of the signal at wavelengths relatively far from the perfect phase matching position (≈ 1600 nm), without a significant CE reduction.

7. CONCLUSIONS

In this work, we presented the design, fabrication and characterization of a fully integrated, IM-FWM-based wavelength

462
463
464
465
466
467
468
469
470
471
472
473
474
475
476
477
478
479
480
481
482
483
484
485
486
487
488
489
490
491
492
493
494
495
496

497

498
499

converter realized on a Si-rich SiN platform. The wavelength converter was designed to operate using a dual-pump BS-IM-FWM configuration that employed the first two horizontal spatial modes (TE_{00} and TE_{10}) of a multimode waveguide. The choice of the Si-rich SiN material provided an additional degree of freedom in the waveguide design compared to standard platforms thanks to the possibility of carefully controlling the refractive index of the deposited layers. In addition, it allowed us to perform nonlinear experiments with relatively high CW pump power levels (>27 dBm), with no sign of detrimental TPA- and free carrier absorption (FCA)-related losses [37,38]. The whole set of mode conversion, multiplexing and demultiplexing functionalities was performed on-chip, with the input/output signals coupled in/out from the chip using two arrays of two lensed single-mode PM optical fibers each. This significantly simplified the experimental setup compared to previous demonstrations of intermodal nonlinearities [12,20,21], reduced the insertion losses of the whole system and removed the requirement to filter out the optical pumps at the output of the device. The system was designed to convert a seeding L-band signal to longer wavelengths by employing optical pumps located in the C- and L-bands. A 3 dB bandwidth for the conversion process exceeding 70 nm was demonstrated, showing the possibility of generating idler components covering the whole U-band. This represents, to the best of the authors' knowledge, the widest bandwidth ever demonstrated for an IM-FWM-based device. The maximum value of the CE was measured to be equal to ≈ -41 dB, mainly limited by the current Si-rich SiN material losses and the relatively short length (1 cm) of the nonlinear multimode waveguide employed in our particular implementation. Comparable CE values were reported in IM-FWM-based wavelength converters implemented in multimode silicon waveguides using CW optical pumps [21–23]. Further improvements in the material quality and fabrication process will result in a significant reduction of the propagation losses of our material, thus enabling the utilization of longer nonlinear multimode waveguides and thereby achieving higher CE values. In this regard, we previously reported CE values as high as -15 dB using a BS-IM-FWM scheme in a Si-rich SiN platform with a different material composition (refractive index of 2.54 at 1550 nm) thanks to the use of a 4 cm long nonlinear multimode waveguide (propagation losses equal to 0.95 dB/cm at 1550 nm), with off-chip optical mode manipu-

lation [20]. Additionally, the implementation of longer low-loss nonlinear waveguide sections would allow the use of lower pump power levels compared to the relatively high ones used in this work (27.6 dBm total pump power). One attractive route for the material optimization is represented by the use of high-temperature ($>1000^\circ\text{C}$) thermal annealing processes, which have been widely exploited to significantly decrease the losses of stoichiometric silicon nitride (Si_3N_4 , refractive index of ≈ 2 at 1550 nm), resulting in waveguide propagation losses lower than 0.05 dB/cm [38,48]. These techniques have already proven to be effective even for Si-rich SiN platforms slightly enriched in the silicon content (refractive index of 2.07 at 1550 nm) compared to Si_3N_4 , with measured propagation losses as low as 0.4 dB/cm [49]. In conclusion, the demonstrated device shows the potential of the BS-IM-FWM phase matching scheme and marks a noteworthy advancement towards the realization of a fully integrated, highly tunable frequency synthesizer capable of operating within optical bands with hundreds of nanometers separation. It is worth noting that, when compared to other IM nonlinear processes, the BS-IM-FWM configuration has the potential to convert photons from the signal to the newly generated idler frequencies without excess noise, entailing far-reaching implications for both classical telecommunications and quantum systems. Appropriate adaptation of the design of the integrated mode-MUX and -DEMUX devices would allow the nonlinear multimode waveguide to operate with higher-order spatial modes, potentially leading to the realization of compact and tunable MIR sources. These developments could hold profound implications across a diverse spectrum of technological applications, encompassing gas sensing [50], molecular spectroscopy [51], medicine and biology [52], free space telecommunication [53] and quantum optics [54].

APPENDIX A: INTEGRATED DEVICE DIMENSIONS

Figure 10 shows a schematic view of the left side of the designed integrated system with the parameter names used to indicate the device dimensions. The right side of the device, not shown in the figure, is a mirrored copy of the left side and has the same dimensions. Table 1 reports the full list of the device geometrical parameters and their respective values.

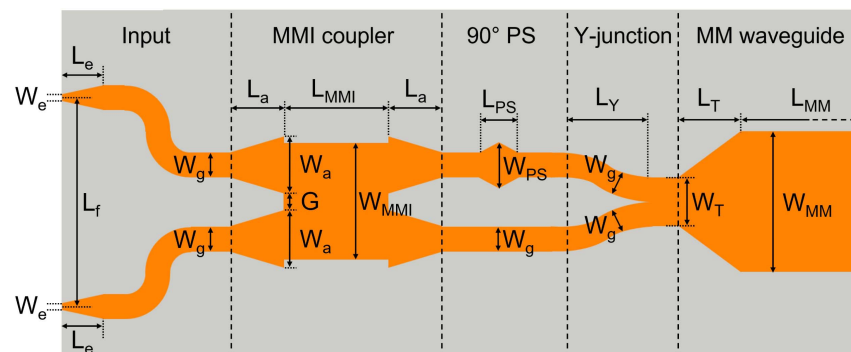


Fig. 10. Schematic view of the left side of the integrated wavelength converter with the parameter names used to indicate the device dimensions. MMI coupler, multimode interference coupler; PS, phase shifter; MM waveguide, multimode waveguide.

Table 1. Device Geometrical Parameters^a

	Component	Parameter	Value
T1:1			
T1:2	SM waveguide	Width	W^g 0.5 μm
T1:3	Input section	Edge coupler tip	W^e 0.228 μm
T1:4		Edge coupler length	L^e 125 μm
T1:5		Input separation	L^f 250 μm
T1:6	MMI coupler	Taper length	L^a 18.5 μm
T1:7		Access width	W^a 1.5 μm
T1:8		Gap	G 1 μm
T1:9		MMI length	L_{MMI} 39.8 μm
T1:10		MMI width	W_{MMI} 3.85 μm
T1:11	90° Phase shifter	PS width	W_{PS} 0.69 μm
T1:12		PS length	L_{PS} 5.2 μm
T1:13	Y-junction	Stem width	W_{T} 1 μm
T1:14		Arm length	L_{Y} 28.64 μm
T1:15	MM waveguide	Taper length	L_{T} 200 μm
T1:16		Waveguide length	L_{MM} 1 cm
T1:17		Waveguide width	W_{MM} 6.1 μm

^aSM waveguide, single-mode waveguide; MMI coupler, multimode interference coupler; PS, phase shifter; MM waveguide, multimode waveguide.

584 **Funding.** Engineering and Physical Sciences Research
585 Council (EP/R003076/1, EP/T007303/1, EP/W024772/1);
586 Ministero dell'Università e della Ricerca (PRIN
587 (2022H7RR4F)).

588 **Acknowledgment.** The use of the IRIDIS High
589 Performance Computing Facility at the University of
590 Southampton is acknowledged. The fabrication was carried
591 out at the Southampton Nanofabrication Centre, part of the
592 Zepler Institute, at the University of Southampton, United
593 Kingdom.

594 **Disclosures.** The authors declare no conflicts of interest.

595 **Data Availability.** Data underlying the results presented
596 in this paper are available from the corresponding author upon
597 reasonable request.

598 REFERENCES

1. D. Dai and J. E. Bowers, "Silicon-based on-chip multiplexing technologies and devices for peta-bit optical interconnects," *Nanophotonics* **3**, 283–311 (2014).
2. I. Cristiani, C. Lacava, G. Rademacher, B. J. Puttnam, R. S. Luis, C. Antonelli, A. Mecozzi, M. Shtaf, D. Cozzolino, D. Bacco, L. K. Oxenl we, J. Wang, Y. Jung, D. J. Richardson, S. Ramachandran, M. Guasoni, K. Krupa, D. Kharenko, A. Tonello, S. Wabnitz, D. B. Phillips, D. Faccio, T. G. Euser, S. Xie, P. St.J. Russell, D. Dai, Y. Yu, P. Petropoulos, F. Gardes, and F. Parmigiani, "Roadmap on multimode photonics," *J. Opt.* **24**, 083001 (2022).
3. Y. Su, Y. He, H. Chen, X. Li, and G. Li, "Perspective on mode-division multiplexing," *Appl. Phys. Lett.* **118**, 200502 (2021).
4. S. Berdagu  and P. Facq, "Mode division multiplexing in optical fibers," *Appl. Opt.* **21**, 1950–1955 (1982).
5. J. Renaudier, A. Napoli, M. Ionescu, C. Calo, G. Fiol, V. Mikhailov, W. Forsysiak, N. Fontaine, F. Poletti, and P. Poggiolini, "Devices and fibers for ultrawideband optical communications," *Proc. IEEE* **110**, 1742–1759 (2022).
6. A. Ferrari, A. Napoli, J. K. Fischer, N. Costa, A. D'Amico, J. Pedro, W. Forsysiak, E. Pincemin, A. Lord, A. Stavdas, J. P. F.-P. Gimenez, G. Roelkens, N. Calabretta, S. Abrate, B. Sommerkorn-Krombholz, and V. Curri, "Assessment on the achievable throughput of multi-band

- ITU-T G.652.D fiber transmission systems," *J. Lightwave Technol.* **38**, 4279–4291 (2020).
7. J. Leuthold, C. Koos, and W. Freude, "Nonlinear silicon photonics," *Nat. Photonics* **4**, 535–544 (2010).
8. M. A. Foster, A. C. Turner, J. E. Sharping, B. S. Schmidt, M. Lipson, and A. L. Gaeta, "Broad-band optical parametric gain on a silicon photonic chip," *Nature* **441**, 960–963 (2006).
9. S. Zlatanovic, J. S. Park, S. Moro, J. M. C. Boggio, I. B. Divliansky, N. Alic, S. Mookherjee, and S. Radic, "Mid-infrared wavelength conversion in silicon waveguides using ultracompact telecom-band-derived pump source," *Nat. Photonics* **4**, 561–564 (2010).
10. A. Ayan, F. Mazeas, J. Liu, T. J. Kippenberg, and C.-S. Br s, "Polarization selective ultra-broadband wavelength conversion in silicon nitride waveguides," *Opt. Express* **30**, 4342–4350 (2022).
11. Y. Franz, J. Haines, C. Lacava, and M. Guasoni, "Strategies for wide-band light generation in nonlinear multimode integrated waveguides," *Phys. Rev. A* **103**, 013511 (2021).
12. S. Signorini, M. Mancinelli, M. Borghi, M. Bernard, M. Ghulinyan, G. Pucker, and L. Pavesi, "Intermodal four-wave mixing in silicon waveguides," *Photon. Res.* **6**, 805–814 (2018).
13. R. Kou, A. Ishizawa, K. Yoshida, N. Yamamoto, X. Xu, Y. Kikkawa, K. Kawashima, T. Aihara, T. Tsuchizawa, G. Cong, K. Hitachi, T. Nishikawa, K. Oguri, and K. Yamada, "Spatially resolved multimode excitation for smooth supercontinuum generation in a SiN waveguide," *Opt. Express* **31**, 6088–6098 (2023).
14. A. ben Khalifa, A. B. Salem, and R. Cherif, "Multimode supercontinuum generation in As₂S₃ chalcogenide photonic crystal fiber," in *Frontiers in Optics* (Optica, 2018), paper JTU2A–18.
15. R. Dupiol, K. Krupa, A. Tonello, M. Fabert, D. Modotto, S. Wabnitz, G. Millot, and V. Couderc, "Interplay of Kerr and Raman beam cleaning with a multimode microstructure fiber," *Opt. Lett.* **43**, 587–590 (2018).
16. Y. Zhang, K. Zhong, G. Hu, D. Yi, R. R. Kumar, and H. K. Tsang, "Sub-milliwatt optical frequency combs in dual-pumped high-Q multimode silicon resonators," *Appl. Phys. Lett.* **117**, 221103 (2020).
17. Y. Zhang, G. Hu, K. Zhong, W. Zhou, and H. K. Tsang, "Investigation of low-power comb generation in silicon microresonators from dual pumps," *J. Opt.* **23**, 10LT03 (2021).
18. Y. Liu, A. Choudhary, G. Ren, D.-Y. Choi, A. Casas-Bedoya, B. Morrison, P. Ma, T. G. Nguyen, A. Mitchell, S. J. Madden, D. Marpaung, and B. J. Eggleton, "Circulator-free Brillouin photonic planar circuit," *Laser Photon. Rev.* **15**, 2000481 (2021).
19. E. A. Kittlaus, N. T. Otterstrom, and P. T. Rakich, "On-chip inter-modal Brillouin scattering," *Nat. Commun.* **8**, 15819 (2017).
20. C. Lacava, T. D. Bucio, A. Khokhar, P. Horak, Y. Jung, F. Gardes, D. Richardson, P. Petropoulos, and F. Parmigiani, "Intermodal frequency generation in silicon-rich silicon nitride waveguides," *Photon. Res.* **7**, 615–621 (2019).
21. C. Lacava, M. A. Ettabib, T. D. Bucio, G. Sharp, A. Z. Khokhar, Y. Jung, M. Sorel, F. Gardes, D. J. Richardson, P. Petropoulos, and F. Parmigiani, "Intermodal Bragg-scattering four wave mixing in silicon waveguides," *J. Lightwave Technol.* **37**, 1680–1685 (2019).
22. S. Signorini, M. Finazzar, M. Bernard, M. Ghulinyan, G. Pucker, and L. Pavesi, "Silicon photonics chip for inter-modal four wave mixing on a broad wavelength range," *Front. Phys.* **7**, 128 (2019).
23. G. Ronniger, I. Sackey, T. Kernetzky, U. H fner, C. Mai, C. Schubert, N. Hanik, L. Zimmermann, R. Freund, and K. Petermann, "Efficient ultra-broadband C-to-O band converter based on multi-mode silicon-on-insulator waveguides," in *European Conference on Optical Communication (ECOC)* (IEEE, 2021), pp. 1–4.
24. S. Liang, Y. Jung, K. R. Bottrill, P. Zhang, D. J. Richardson, and L. Xu, "L-band mode and wavelength conversion in a periodically poled lithium niobate ridge waveguide," in *European Conference and Exhibition on Optical Communication* (Optica, 2022), paper Tu5-22.
25. S. Signorini, M. Sanna, S. Piccione, M. Ghulinyan, P. Tidemand-Lichtenberg, C. Pedersen, and L. Pavesi, "A silicon source of heralded single photons at 2 μm ," *APL Photon.* **6**, 126103 (2021).
26. L.-T. Feng, M. Zhang, X. Xiong, Y. Chen, H. Wu, M. Li, G.-P. Guo, G.-C. Guo, D.-X. Dai, and X.-F. Ren, "On-chip transverse-mode-entangled photon pair source," *npj Quantum Inf.* **5**, 2 (2019).

621
622
623
624
625
626
627
628
629
630
631
632
633
634
635
636
637
638
639
640
641
642
643
644
645
646
647
648
649
650
651
652
653
654
655
656
657
658
659
660
661
662
663
664
665
666
667
668
669
670
671
672
673
674
675
676
677
678
679
680
681
682
683
684
685
686
687
688
689
690
691

- 692 27. S. Paesani, M. Borghi, S. Signorini, A. Maïnos, L. Pavesi, and A.
693 Laing, "Near-ideal spontaneous photon sources in silicon quantum
694 photonics," *Nat. Commun.* **11**, 2505 (2020).
- 695 28. C. J. McKinstrie, S. Radic, and M. Raymer, "Quantum noise properties
696 of parametric amplifiers driven by two pump waves," *Opt. Express* **12**,
697 5037–5066 (2004).
- 698 29. C. McKinstrie, M. Yu, M. Raymer, and S. Radic, "Quantum noise prop-
699 erties of parametric processes," *Opt. Express* **13**, 4986–5012 (2005).
- 700 30. C. McKinstrie, J. Harvey, S. Radic, and M. Raymer, "Translation of
701 quantum states by four-wave mixing in fibers," *Opt. Express* **13**,
702 9131–9142 (2005).
- 703 31. Q. Li, M. Davanço, and K. Srinivasan, "Efficient and low-noise single-
704 photon-level frequency conversion interfaces using silicon nanophoto-
705 nics," *Nat. Photonics* **10**, 406–414 (2016).
- 706 32. I. Agha, S. Ates, M. Davanço, and K. Srinivasan, "A chip-scale, tele-
707 communications-band frequency conversion interface for quantum
708 emitters," *Opt. Express* **21**, 21628–21638 (2013).
- 709 33. A. C. Turner, C. Manolatu, B. S. Schmidt, M. Lipson, M. A. Foster,
710 J. E. Sharping, and A. L. Gaeta, "Tailored anomalous group-velocity
711 dispersion in silicon channel waveguides," *Opt. Express* **14**, 4357–
712 4362 (2006).
- 713 34. K. Li, H. Sun, and A. C. Foster, "Four-wave mixing Bragg scattering in
714 hydrogenated amorphous silicon waveguides," *Opt. Lett.* **42**, 1488–
715 1491 (2017).
- 716 35. F. Parmigiani, P. Horak, Y. Jung, L. Grüner-Nielsen, T. Geisler, P.
717 Petropoulos, and D. Richardson, "All-optical mode and wavelength
718 converter based on parametric processes in a three-mode fiber,"
719 *Opt. Express* **25**, 33602–33609 (2017).
- 720 36. S. M. M. Friis, I. Begleris, Y. Jung, K. Rottwitz, P. Petropoulos, D.
721 Richardson, P. Horak, and F. Parmigiani, "Inter-modal four-wave mix-
722 ing study in a two-mode fiber," *Opt. Express* **24**, 30338–30349 (2016).
- 723 37. C. Lacava, S. Stankovic, A. Z. Khokhar, T. D. Bucio, F. Gardes, G. T.
724 Reed, D. J. Richardson, and P. Petropoulos, "Si-rich silicon nitride for
725 nonlinear signal processing applications," *Sci. Rep.* **7**, 22 (2017).
- 726 38. F. Gardes, A. Shooa, G. De Paoli, I. Skandalos, S. Ilie, T. Rutirawut,
727 W. Talataisong, J. Faneca, V. Vitali, Y. Hou, T. Domínguez Bucio, I.
728 Zeimpekis, C. Lacava, and P. Petropoulos, "A review of capabilities
729 and scope for hybrid integration offered by silicon-nitride-based pho-
730 tonic integrated circuits," *Sensors* **22**, 4227 (2022).
- 731 39. E. D. Palik, *Handbook of Optical Constants of Solids* (Academic,
732 1998), Vol. **3**.
- 733 40. P. Horak and F. Poletti, "Multimode nonlinear fibre optics: theory and
734 applications," in *Recent Progress in Optical Fiber Research*
735 (IntechOpen, 2012), Vol. **3**.
- 736 41. D. González-Andrade, J. G. Wangüemert-Pérez, A. V. Velasco, A.
737 Ortega-Monux, A. Herrero-Bermello, I. Molina-Fernandez, R. Halir,
738 and P. Cheben, "Ultra-broadband mode converter and multiplexer
739 based on sub-wavelength structures," *IEEE Photon. J.* **10**,
740 2201010 (2018).
- 741 42. D. González-Andrade, A. Dias, J. G. Wangüemert-Pérez, A. Ortega-
742 Moñux, Í. Molina-Fernández, R. Halir, P. Cheben, and A. V. Velasco,
743 "Experimental demonstration of a broadband mode converter and
744 multiplexer based on subwavelength grating waveguides," *Opt.*
745 *Laser Technol.* **129**, 106297 (2020).
- 746 43. T. D. Bucio, A. Z. Khokhar, C. Lacava, S. Stankovic, G. Z.
747 Mashanovich, P. Petropoulos, and F. Y. Gardes, "Material and optical
748 properties of low-temperature NH₃-free PECVD SiNx layers for pho-
749 tonic applications," *J. Phys. D* **50**, 025106 (2016).
- 750 44. L. Carpenter, S. Berry, and C. Gawith, "Ductile dicing of LiNbO₃ ridge
751 waveguide facets to achieve 0.29 nm surface roughness in single pro-
752 cess step," *Electron. Lett.* **53**, 1672–1674 (2017).
- 753 45. P. C. Gow, G. M. Churchill, V. Vitali, T. D. Bucio, P. Petropoulos, F. Y.
754 Gardes, C. B. Gawith, and J. C. Gates, "Ductile dicing for optical fac-
755 ets and waveguides in silicon nitride," in *Conference on Lasers and*
756 *Electro-Optics Europe & European Quantum Electronics*
757 *Conference (CLEO/Europe-EQEC)* (IEEE, 2023).
- 758 46. D. González-Andrade, R. F. de Cabo, J. Vilas, I. Olivares, A. Dias,
759 J. M. Luque-González, J. G. Wangüemert-Pérez, A. Ortega-Moñux,
760 Í. Molina-Fernández, R. Halir, P. Cheben, and A. V. Velasco,
761 "Mode converter and multiplexer with a subwavelength phase shifter
762 for extended broadband operation," *IEEE Photon. Technol. Lett.* **33**,
763 1262–1265 (2021).
- 764 47. D. González-Andrade, J. M. Luque-González, J. G. Wangüemert-
765 Pérez, A. Ortega-Moñux, P. Cheben, Í. Molina-Fernández, and
766 A. V. Velasco, "Ultra-broadband nanophotonic phase shifter based
767 on subwavelength metamaterial waveguides," *Photon. Res.* **8**,
768 359–367 (2020).
- 769 48. Z. Ye, P. Zhao, K. Twayana, M. Karlsson, V. Torres-Company, and
770 P. A. Andrekson, "Overcoming the quantum limit of optical amplifica-
771 tion in monolithic waveguides," *Sci. Adv.* **7**, eabi8150 (2021).
- 772 49. Z. Ye, A. Fülöp, Ó. B. Helgason, P. A. Andrekson, and V. Torres-
773 Company, "Low-loss high-Q silicon-rich silicon nitride microresona-
774 tors for Kerr nonlinear optics," *Opt. Lett.* **44**, 3326–3329 (2019).
- 775 50. D. Popa and F. Udrea, "Towards integrated mid-infrared gas sensors,"
776 *Sensors* **19**, 2076 (2019).
- 777 51. M. Vainio and L. Halonen, "Mid-infrared optical parametric oscillators
778 and frequency combs for molecular spectroscopy," *Phys. Chem.*
779 *Chem. Phys.* **18**, 4266–4294 (2016).
- 780 52. K. Isensee, N. Kröger-Lui, and W. Petrich, "Biomedical applications of
781 mid-infrared quantum cascade lasers—a review," *Analyst* **143**, 5888–
782 5911 (2018).
- 783 53. Y. Su, W. Wang, X. Hu, H. Hu, X. Huang, Y. Wang, J. Si, X. Xie, B.
784 Han, H. Feng, Q. Hao, G. Zhu, T. Duan, and W. Zhao, "10 Gbps
785 DPSK transmission over free-space link in the mid-infrared," *Opt.*
786 *Express* **26**, 34515–34528 (2018).
- 787 54. L. M. Rosenfeld, D. A. Sulway, G. F. Sinclair, V. Anant, M. G.
788 Thompson, J. G. Rarity, and J. W. Silverstone, "Mid-infrared quantum
789 optics in silicon," *Opt. Express* **28**, 37092–37102 (2020).

Queries

790

1. AU: The funding information for this article has been generated using the information you provided at the time of article submission. Please check it carefully. If any information needs to be corrected or added, please provide the full name of the funding organization/institution as provided in the CrossRef Open Funder Registry (<https://search.crossref.org/funding>).